Chemical Science

Accepted Manuscript

This article can be cited before page numbers have been issued, to do this please use: Z. Wan, W. Yu, J. Yang, Y. Zhang, Y. Wang, R. Wei, M. Azam, J. Luo and C. Jia, *Chem. Sci.*, 2025, DOI: 10.1039/D5SC04440E.

ROYAL SOCIETY OF CHEMISTRY

rsc.li/chemical-science

View Article Online
DOI: 10.1039/D5SC04440E

Non-ionic fluorinated p-dopant enables efficient and stable perovskite solar cells

Zhongquan Wan*, Wang Yu, Jinyu Yang, Yunpeng Zhang, Yuanxi Wang, Runmin Wei, Muhammad Azam, Junsheng Luo*, Chunyang Jia*

National Key Laboratory of Electronic Films and Integrated Devices, School of Integrated Circuit Science and Engineering, University of Electronic Science and Technology of China, 611731 Chengdu, P. R. China

*Correspondence to: zqwan@uestc.edu.cn, luojs@uestc.edu.cn, cyjia@uestc.edu.cn

Abstract: Li-TFSI/t-BP system is essential for doping hole-transporting layer (HTL) to construct efficient perovskite solar cells (PSCs). However, the hygroscopicity and Li^+ migration of Li-TFSI, as well as the corrosiveness and volatility of t-BP, can have negative impacts on the efficiency and stability of PSCs. Herein, a novel non-ionic fluorinated p-dopant 1-[bis (trifluoromethanesulfonyl) methyl]-2,3,4,5,6-pentafluorobenzene (PFB-TFSI) is developed to replace Li-TFSI/t-BP system. The non-ionic structure of PFB-TFSI allows it to dissolve in chlorobenzene without t-BP. Moreover, due to the lower HOMO level of PFB-TFSI, it can directly oxidize PTAA to generate $[PTAA]^+$ radical cations without post-treatment, achieving effective doping of PTAA. The moisture resistance of HTL is also improved due to the presence of multiple fluorine atoms in PFB-TFSI. Ultimately, compared to 21.98% efficiency of PSC based on PTAA:Li-TFSI/t-BP, PSC based on PTAA:PFB-TFSI achieved higher efficiency (24.22%). Furthermore, the long-term stability of PSC based on PTAA:PFB-TFSI is greatly improved, retaining 88% of the initial efficiency after aging for 300 hours at 85 °C and 50-70% relative humidity, whereas PSC based on PTAA:Li-TFSI/t-BP only retains 63%.

Keywords: Perovskite solar cells; Hole-transporting layer; p-Dopant; Fluorinated molecule; Long-term stability

View Article Online
DOI: 10.1039/D5SC04440E

1. Introduction

Organic-inorganic hybrid perovskite solar cells have experienced rapid development due to their advantages such as high photovoltaic conversion efficiency, simple fabrication process, tunable direct bandgap, high charge carrier mobility, long diffusion length, and relatively low cost. The photovoltaic conversion efficiency (PCE) of PSCs has increased from 3.8% to 26.95%[1-6]. In PSCs, the hole-transporting layer (HTL) effectively blocks electrons while collecting holes, achieving efficient electron-hole separation. Simultaneously, it impedes moisture diffusion into PSCs, reducing degradation caused by moisture in the air[7-10].

Presently, PTAA and Spiro-OMeTAD are used as classic HTL materials in PSCs[11]. However, their intrinsic hole mobility and conductivity are low, necessitating the addition of hole doping agents to enhance p-type doping and improve hole-transporting performance to increase PSCs' efficiency[12]. The most widely used doping system currently is the Li-TFSI/t-BP system. t-BP facilitates the dissolution of Li-TFSI in non-polar solutions like chlorobenzene. Li-TFSI does not directly dope but promotes oxidative doping of the HTM under sunlight[13-15]. While achieving high efficiency, the Li-TFSI/t-BP system also brings negative issues: Li^+ has a small ion radius, and easily to diffuse to the other layer, and has strong hygroscopicity which can absorb moisture from the air and damage the perovskite layer[16, 17]. Meanwhile, the polar solvent t-BP with low boiling point will evaporate in HTL, leaving voids and damaging perovskite layer[18-20]. Besides, Indirect doping is highly dependent on environmental conditions, time-consuming, and lacks repeatability[21]. These issues degrade the performance and stability of PSCs and hinder their commercialization[22]. Current works are focused on solving the problems caused by hygroscopic Li^+[23-25]. For instance, strategies include adding small amounts of PbI_2 to the Li-TFSI/t-BP system to inhibit Li-TFSI aggregation and t-BP evaporation[26], incorporating reduced graphene oxide to mitigate Li^+ ion hygroscopicity[27], and introducing MoS_2 to absorb Li^+ ions and suppress their migration[28]. However, extra additives bring new challenges and increase costs and

complexity. Therefore, developing stable and efficient p-dopants to replace Li-TFSI/t-BP system remains a better choice[29].

In this study, a novel fluorinated molecule 1-[bis (trifluoromethanesulfonyl) methyl]-2,3,4,5,6-pentafluorobenzene (PFB-TFSI) is developed as a p-dopant (Figure 1a). Serving as a non-ionic p-dopant, PFB-TFSI addresses issues related to Li^+ ion migration and hygroscopicity. Unlike Li-TFSI, it can dissolve directly in chlorobenzene without t-BP, and the positive charges on the molecular surface are more concentrated (Figure 1b), giving the molecule Lewis acid properties that facilitate the spontaneous transfer of charges to form hole states, achieving effective p-type doping. Furthermore, PFB-TFSI possesses a suitable HOMO energy level to accommodate electron transfer within PTAA, enabling direct oxidation to yield $[PTAA]^+$ radical cations under anaerobic conditions. Ultimately, PSC utilizing PTAA:PFB-TFSI achieved a PCE of 24.22%, while exhibiting good stability under unencapsulated atmospheric conditions.

2. Results and Discussion

Initially, PFB-TFSI and Li-TFSI/t-BP were dissolved in PTAA solution separately. The color of the PTAA solution immediately turned brown after adding PFB-TFSI, while the solution with Li-TFSI/t-BP remained light yellow (Figure 1d). The change in color informs that charge transfer may has occurred in the solution, which preliminarily indicates PFB-TFSI directly achieves p-type doping of PTAA, generating $[PTAA]^+$ radical cations. To confirm the conclusion, UV-visible absorption and electron spin resonance (ESR) were conducted. The PTAA:PFB-TFSI solution exhibits a new strong absorption peak near 540 nm compared to undoped PTAA solution (Figure 1d), which is attributed to the direct oxidation process of PFB-TFSI, while the PTAA:Li-TFSI/t-BP solution only shows a very weak absorption peak near 540 nm. Moreover, PTAA:PFB-TFSI solution shows a strong $[PTAA]^+$ radical signal at 3500-3520G (Figure 1e), confirming the presence of $[PTAA]^+$ radical cations[30, 31]. From the above analysis, it can be concluded that PTAA can be doped with PFB-TFSI in an anaerobic environment without t-BP and acetonitrile, generating $[PTAA]^+$ radical cations in the solution.

View Article Online
DOI: 10.1039/D5SC04440E

To verify the intermolecular charge transfer, the differential charge of PTAA:PFB-TFSI was calculated, and the PTAA structure has been replaced by trimers for ease of calculation, where blue and red represent charge accumulation and depletion respectively (Figure 1c). When PFB-TFSI interacts with PTAA, the electrons are mainly concentrated on PFB-TFSI, while the holes are primarily concentrated at the interface between PTAA and PFB-TFSI, which indicates the presence of charge transfer between PFB-TFSI and PTAA. Furthermore, the conductivity of the HTL was tested to evaluate the doping effect of different dopants on PTAA (Figure 1f). Compared to the PTAA:Li-TFSI/t-BP film (8.87×10^{-6} S/cm), PTAA:PFB-TFSI film exhibits higher conductivity (9.95×10^{-6} S/cm), which further confirms that PFB-TFSI can directly oxidize PTAA to generate $[PTAA]^{+}$ radical cations, achieving more effective doping of PTAA.

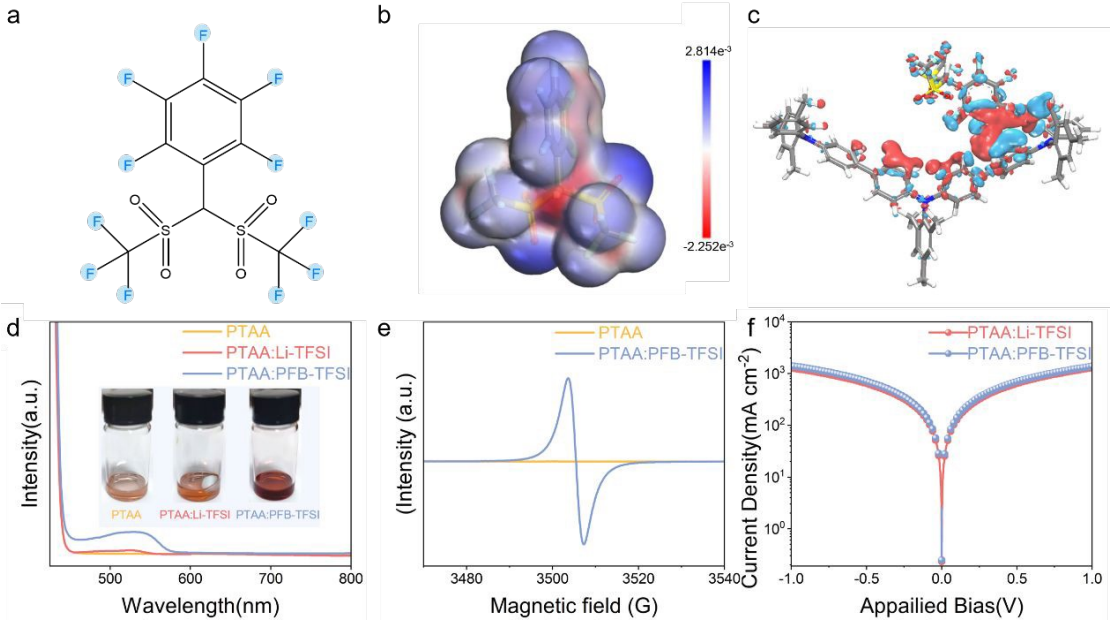

Figure 1. (a) Chemical structure of PFB-TFSI. (b) ESP surface of PFB-TFSI. (c) Differential charge diagram of PTAA:PFB-TFSI. (d) UV-vis absorption spectra of PTAA, PTAA:Li-TFSI/t-BP and PTAA:PFB-TFSI solutions. The illustration shows the color of PTAA solution treated with different dopants. (e) ESR spectra of PTAA:Li-TFSI/t-BP and PTAA:PFB-TFSI solutions. (f) Conductivity tests of PTAA:Li-TFSI/t-BP and PTAA:PFB-TFSI films.

To investigate the doping mechanism of PFB-TFSI on PTAA, the highest occupied molecular orbital (HOMO) energy levels of PFB-TFSI and PTAA were measured using

View Article Online
DOI: 10.1039/D5SC04440E

cyclic voltammetry (CV). As shown in Figure S1, based on the first oxidation potentials (E_{ox}), the HOMO energy levels can be calculated using formula (1):

$$E_{HOMO} = -(E_{ox} + 4.70) \quad (1)$$

where the values of E_{ox} for PFB-TFSI and PTAA were 0.62 and 0.55 V, and the corresponding HOMO energy levels were calculated to be -5.32 and -5.25 eV, respectively. The lower HOMO energy level of PFB-TFSI facilitates direct electron transfer from PTAA, indicating that PFB-TFSI can directly oxidize PTAA to generate $[PTAA]^+$ under anaerobic condition, thereby avoiding the subsequent slow oxidation step. In addition, as shown in Figure S1, compared with the E_{ox} of PTAA and PFB-TFSI solutions, the E_{ox} of PTAA:PFB-TFSI mixture solution changed (0.58 V), indicating charge transfer between PTAA and PFB-TFSI. The above experiments and theoretical calculations demonstrate that PFB-TFSI can be used for direct oxidation of PTAA[32, 33].

Introducing PFB-TFSI into HTL can regulate the HOMO energy level, promote the energy level alignment between HTL and perovskite, and thus improve charge carrier transport efficiency. In order to elucidate the regulatory effect of two different p-dopants on the HOMO energy level of PTAA, the PTAA films with different p-dopants were further characterized using ultraviolet photoelectron spectroscopy (UPS). Figures 2a and 2b show the UPS spectra of PTAA films doped with different p-dopants, including the cutoff (E_{cutoff}) and onset (E_{onset}) energy regions. The position of the HOMO energy level can be calculated using formula (2):

$$E_{HOMO} = h\nu - (E_{cutoff} - E_{onset}) \quad (2)$$

where $h\nu$ is the He(I) photon energy (21.22 eV). Ultimately, the HOMO energy level of PTAA:PFB-TFSI film was calculated as -5.10 eV, indicating a certain degree of reduction compared to the PTAA:Li-TFSI/t-BP (-5.01 eV)[34, 35]. As shown in the energy level diagram (Figure 2c), the lower HOMO energy level optimizes the energy level alignment between the perovskite layer and HTL, reduces the Schottky barrier, and thus

reduces energy loss during hole extraction, ultimately leading to higher open-circuit voltage (V_{oc}).

To further investigate charge transfer at the interface, steady-state photoluminescence (PL) and transient photoluminescence (TRPL) were employed to study the hole extraction capability between the perovskite layer and HTL. From the PL spectra shown in Figure 2d, it can be seen that the emission peak intensity at 764 nm shows the order of glass/perovskite > glass/perovskite/PTAA:Li-TFSI/t-BP > glass/perovskite/PTAA:PFB-TFSI samples, indicating that PFB-TFSI doping enhances hole extraction from the perovskite. Moreover, compared to glass/perovskite/PTAA:Li-TFSI/t-BP sample, the PL peak of glass/perovskite/PTAA:PFB-TFSI sample exhibited a blue shift (PL peak shifted from 760 nm to 764 nm), which is due to PFB-TFSI not only having a doping effect on PTAA but also passivating defect states on the perovskite surface[36].

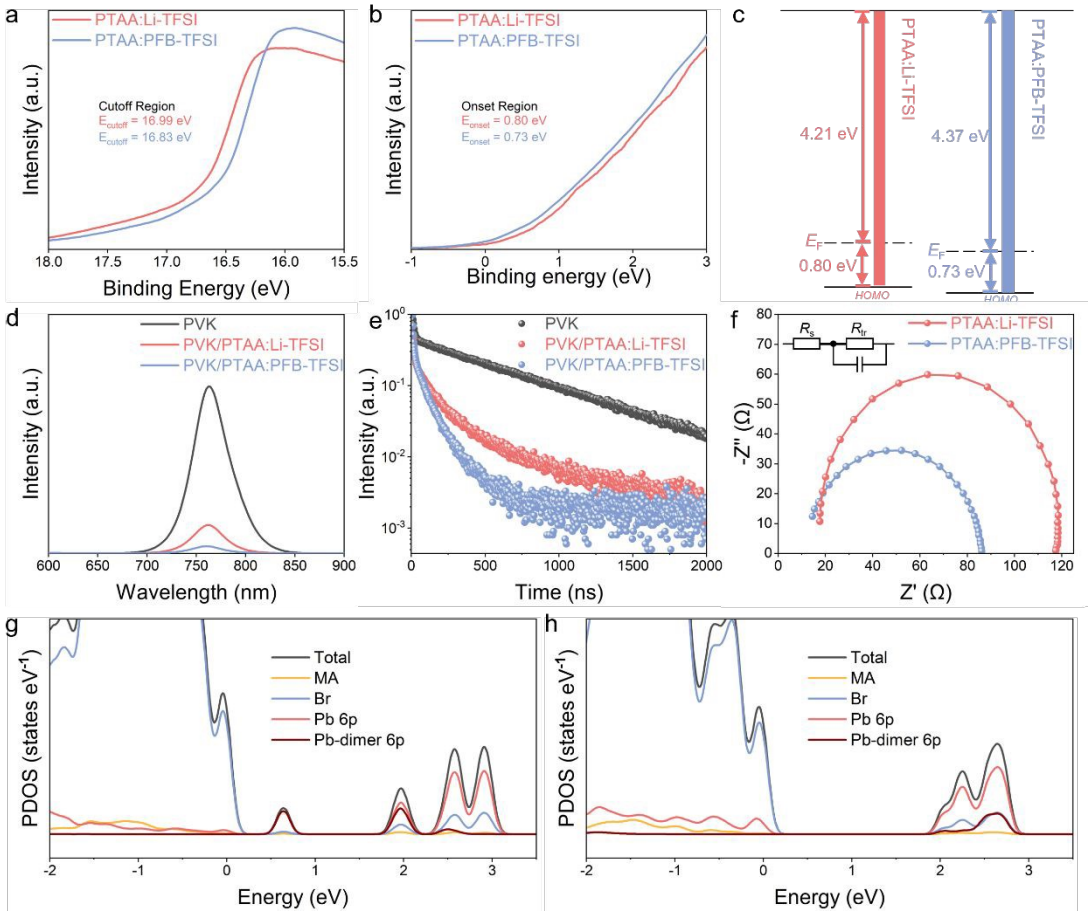

Figure 2. (a) Cutoff regions and (b) onset regions of the UPS spectra for PTAA:Li-TFSI/t-BP and

PTAA:PFB-TFSI films. (c) Energy level diagrams of PTAA:Li-TFSI/t-BP and PTAA:PFB-TFSI films. (d) Steady-state PL and (e) TRPL spectra of glass/perovskite, glass/perovskite/PTAA:Li-TFSI/t-BP and glass/perovskite/PTAA:PFB-TFSI samples. (f) Nyquist plots of PSCs based on PTAA:Li-TFSI/t-BP and PTAA:PFB-TFSI. PDOS diagrams of Pb-Pb dimer defects (g) before and (h) after PFB-TFSI absorption.

Figure 2e shows the TRPL spectra for the samples with the same structure in PL spectra. The average decay time τ_{ave} was fitted with a three exponential decay model. The glass/perovskite sample exhibits the longest τ_{ave} of 597.2 ns, while the τ_{ave} of glass/perovskite/PTAA:Li-TFSI/t-BP sample is 92.08 ns. The τ_{ave} of glass/perovskite/PTAA:PFB-TFSI is further reduced (41.91 ns), indicating that HTL doped with PFB-TFSI has enhanced hole extraction capability. This suggests that PTAA doped with PFB-TFSI can extract and collect holes faster than PTAA doped Li-TFSI/t-BP[37].

Electrochemical impedance spectroscopy (EIS) was utilized to investigate charge transfer processes in perovskite/HTL interface[38]. EIS measurements were performed on PSCs based on PTAA:Li-TFSI/t-BP and PTAA:PFB-TFSI, and results were fitted using ZView software (Figure 2f). In the impedance equivalent circuit, R_s represents the series resistance, reflecting the impedance during charge transport within the device, while R_{tr} represents the charge transport resistance at perovskite/HTL interface. Compared to PSC based on PTAA:Li-TFSI/t-BP (R_s =19 Ω; R_{tr} = 99 Ω), PSC based on PTAA:PFB-TFSI has lower R_s (12 Ω) and R_{tr} (75 Ω), attributed to the lower HOMO energy level of PTAA:PFB-TFSI film, which optimizes the energy level alignment and improves charge transport. The low R_s and R_{tr} are beneficial for PSCs to achieve higher fill factor (FF) and PCE.

The numerous defects on the surface of perovskite can serve as recombination centers for charge carriers, affecting hole extraction and transport[39]. Reducing the defects is beneficial for enhancing the hole extraction capability at the perovskite/HTL interface[40]. To investigate the passivation effect of PFB-TFSI on perovskite/HTL interface defects, a Pb-Pb dimer was placed at the perovskite (001) interface to simulate deep-level defect states on the perovskite surface. Figure 2g shows the projected density

View Article Online
DOI: 10.1039/D5SC04440E

of states (PDOS) diagram of the perovskite (001) crystal plane with the Pb-Pb dimer. The addition of the Pb-Pb dimer introduces a deep-level defect in the perovskite bandgap, capturing holes at the perovskite/HTL interface, thus degrading carrier transport performance[41]. The differential charge diagram in Figure S2 also shows similar results, with excess charges on the perovskite surface mainly concentrated around the Pb-Pb dimer, acting as non-radiative recombination centers for photogenerated carriers. However, when PFB-TFSI interacts with the Pb-Pb dimer, the fluorine and oxygen elements in PFB-TFSI interact with the Pb-Pb dimer, causing it to shift from the equilibrium position towards the interior of the perovskite (Figures S3 and S4), thereby suppressing surface charge accumulation. As shown in Figure S5, excess charge on the perovskite surface are transferred to PFB-TFSI. The interaction between PFB-TFSI and the Pb-Pb dimer converts the deep-level defect into a shallow-level defect, causing the gap defect state composed of the Pb-Pb dimer to disappear (Figure 2h), effectively reducing non-radiative recombination, enhancing hole-transporting capability and consequently improving photovoltaic performance of PSCs.

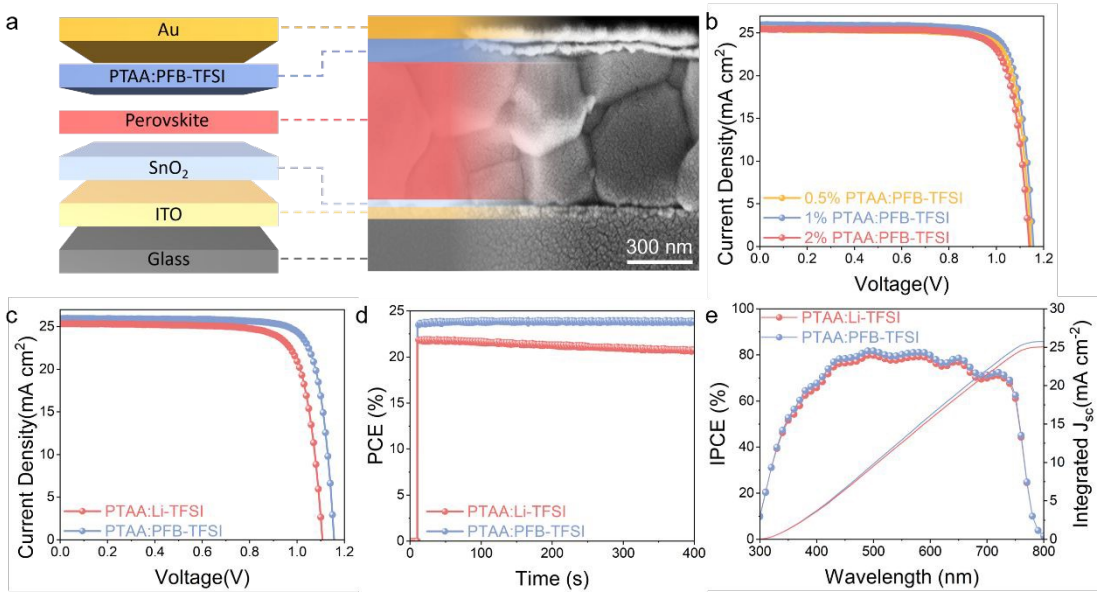

Figure 3. (a) Cross-section SEM of PSC based on ITO/SnO_2/perovskite/PTAA:PFB-TFSI/Au. (b) *J-V* curves of champion efficiency of PSCs based on PTAA doped with various concentrations of PFB-TFSI. (c) *J-V* curves of champion efficiency of PSCs based on PTAA:Li-TFSI/t-BP and PTAA:PFB-TFSI. (d) Steady-state PCE outputs at the MPP for PSCs based on PTAA:Li-TFSI/t-BP and PTAA:PFB-TFSI. (e) IPCE spectra and integrated current densities for PSCs based on

View Article Online
DOI: 10.1039/D5SC04440E

PTAA:Li-TFSI/t-BP and PTAA:PFB-TFSI.

To investigate the impact of PFB-TFSI on the photovoltaic performances of PSCs, PSCs with varying concentrations of PFB-TFSI doping were prepared with an ITO/SnO_2/perovskite/PTAA:PFB-TFSI/Au device structure. Figure 3a shows the cross-section SEM of entire device. The *J-V* curves under standard simulated sunlight conditions were tested (Figure 3b), with detailed corresponding data in Table S1. The PCE of PSCs shows an initial increase and then a decrease with the rise in PFB-TFSI doping concentration. The highest PCE of 24.22% (V_{oc} = 1.16 V, J_{sc} = 25.97 mA/cm², FF = 0.804) was achieved at a doping concentration of 1 mol%, which is superior to the PCE of PSC based on PTAA:Li-TFSI/t-BP (PCE = 21.98%, V_{oc} = 1.11 V, J_{sc} = 25.35 mA/cm², FF = 0.781) (Figure 3c). The higher PCE of PSC based on PTAA:PFB-TFSI is primarily attributed to its better energy level alignment and the passivation of perovskite surface defects by PFB-TFSI[42, 43].

Moreover, measurements of the steady-state PCE at the maximum power point under continuous solar illumination further verified the reliability of the photovoltaic performance (Figure 3d). Compared to PSC based on PTAA:Li-TFSI/t-BP, PSC based on PTAA:PFB-TFSI demonstrated faster photoelectric response and superior steady-state output capability. The incident photon-to-electron conversion efficiency (IPCE) for PSCs based on PTAA:Li-TFSI/t-BP and PTAA:PFB-TFSI was examined to confirm the accuracy of J_{sc} values of PSCs. As shown in Figure 3e, the calculated integrated J_{sc} value of PSC based on PTAA:PFB-TFSI was 25.76 mA/cm², which was in good agreement with the J_{sc} value obtained from experimental *J-V* measurement. Moreover, PSC based on PTAA:PFB-TFSI exhibits higher IPCE than PSC based on PTAA:Li-TFSI/t-BP across the entire visible light spectrum.

View Article Online
DOI: 10.1039/D5SC04440E

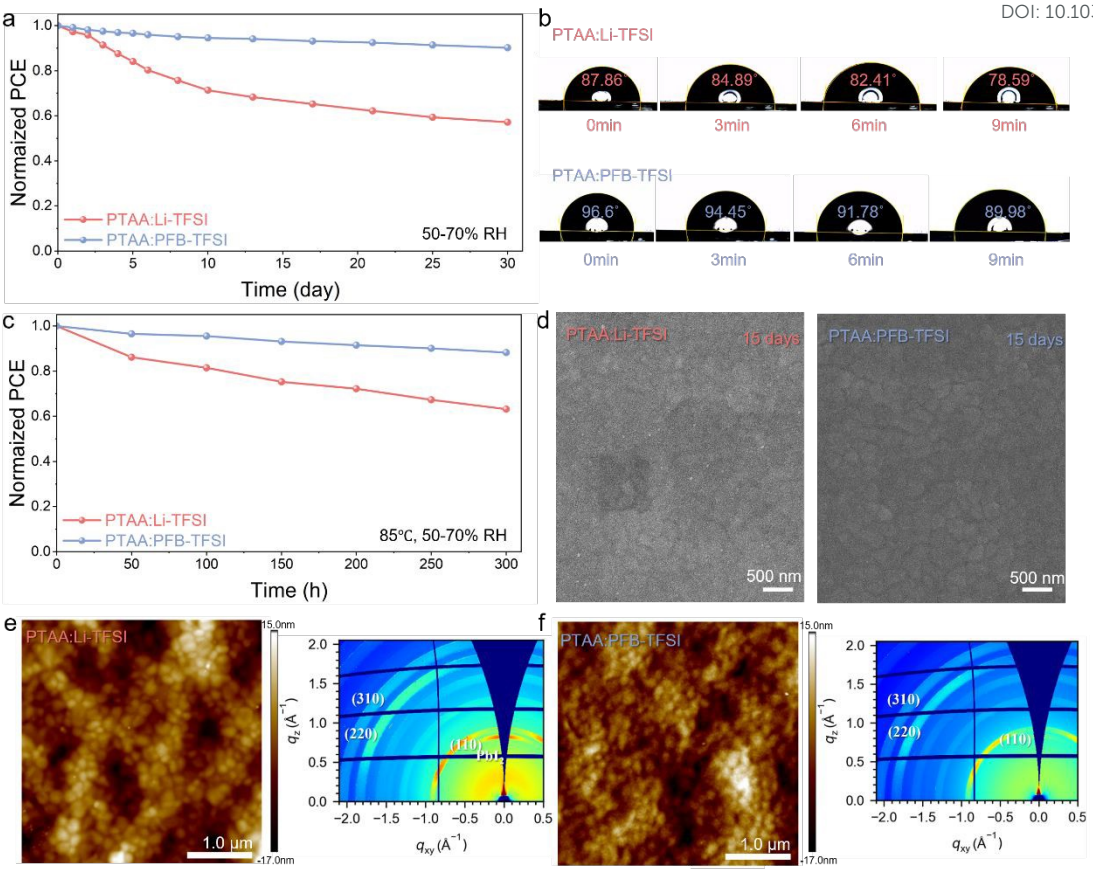

Figure 4. (a) Moisture stability of unencapsulated PSCs based on PTAA:Li-TFSI/t-BP and PTAA:PFB-TFSI. (b) Water contact angles of PTAA:Li-TFSI/t-BP and PTAA:PFB-TFSI films. (c) Damp thermal stability of unencapsulated PSCs based on PTAA:Li-TFSI/t-BP and PTAA:PFB-TFSI. (d) SEM images of the aged PTAA:Li-TFSI/t-BP and PTAA:PFB-TFSI films. AFM topographical images and 2D-GIXD images of (e) aged PTAA:Li-TFSI/t-BP film and (f) aged PTAA:PFB-TFSI film on perovskite layer.

In addition to improving photovoltaic performance, PFB-TFSI also significantly enhances the long-term stability of PSCs. As shown in Figure 4a, the unpackaged PSC based on PTAA:PFB-TFSI maintained 90% of the initial PCE after aging for 30 days in ambient air conditions (23 ± 4 °C, 50-70% relative humidity), while the unpackaged PSC based on PTAA:Li-TFSI/t-BP only retained 57% of the initial PCE under the same conditions. The long-term stability under high temperature and high humidity conditions is crucial for evaluating the stability of PSCs. Therefore, we conducted damp heat stability tests on unpackaged PSCs continuously heated at 85 °C in ambient air with 50-70% relative humidity. As shown in Figure 4c, after aging for 300 hours, the

View Article Online
DOI: 10.1039/D5SC04440E

PSC based on PTAA:PFB-TFSI maintained 88% of its initial PCE, while the PSC based on PTAA:Li-TFSI/t-BP retained only 63% of its initial PCE. The improved long-term stability of PSC based on PTAA:PFB-TFSI is mainly attributed to: 1. PFB-TFSI itself having excellent hydrophobicity, which enhances the hydrophobicity of the HTL and reduces the erosion of perovskite by water molecules; 2. PFB-TFSI being able to passivate the surface defects of the perovskite, slowing down the aging and degradation of the perovskite.

As depicted in Figure S6, when Li-TFSI is placed on the surface of perovskite and exposed to the ambient environment, hygroscopic Li-TFSI absorbs moisture from the air, leading to significant degradation of the perovskite film. Additionally, the polar solvent t-BP can also damage the perovskite film. In contrast, PFB-TFSI, being non-hygroscopic, does not affect the underlying perovskite layer even after being exposed to the ambient environment for 30 days.

Further measurements of the water contact angles of Li-TFSI/t-BP and PFB-TFSI doped PTAA films were conducted to study the hydrophobic properties (Figure 4b). The initial water contact angle of the PTAA:Li-TFSI/t-BP film was 87.86°, due to Li-TFSI absorbing moisture from the air, the contact angle decreased to 78.26° after 9 minutes. In contrast, owing to the excellent hydrophobicity of PFB-TFSI, the initial water contact angle of PTAA:PFB-TFSI film reached 96.6°. After being exposed to the ambient environment for 9 minutes, the water contact angle remains at 89.98°. This demonstrates that compared to PTAA:Li-TFSI/t-BP film, PTAA:PFB-TFSI film exhibits superior hydrophobicity and stability, effectively preventing moisture from infiltrating the perovskite layer[44].

Moreover, to visually assess the impact of PTAA film morphology on the performance and stability of PSCs, AFM and SEM images were obtained for PTAA:Li-TFSI/t-BP and PTAA:PFB-TFSI films. First, SEM images of freshly prepared PTAA:Li-TFSI/t-BP and PTAA:PFB-TFSI films were taken (Figure S7). Due to the hygroscopic nature of Li-TFSI, moisture easily infiltrates the underlying layers. SEM images of PTAA:Li-TFSI/t-BP and PTAA:PFB-TFSI films after aging for 15 days at 23 ± 4 °C in ambient air with 50-70% relative humidity were taken and shown in Figure

View Article Online
DOI: 10.1039/D5SC04440E

4d. Numerous white fluffy substances and pores were clearly observed on the PTAA:Li-TFSI/t-BP film. The former are byproducts of the oxidation process, denoted as Li_xO_y, while the latter are pores left by the volatilization of t-BP, providing pathways for moisture intrusion into the perovskite. These factors contribute to the inferior stability of the HTL doped with Li-TFSI/t-BP. In contrast, due to the non-hygroscopic nature of PFB-TFSI, the PTAA:PFB-TFSI film maintains its original morphology well after aging for 15 days under the same conditions. As shown in the AFM images in Figures 4e and 4f, the root mean square (RMS) of PTAA:Li-TFSI/t-BP film reaches 7.07 nm, while the surface RMS of PTAA:PFB-TFSI film is only 5.88 nm. Additionally, the Kelvin Probe Force Microscopy (KPFM) was performed to characterize the surface potentials of PTAA:Li-TFSI/t-BP and PTAA:PFB-TFSI films (Figure S8). The distribution of surface potential and average value have been exhibited. The average surface potential of PTAA:PFB-TFSI film (25 mV) is lower than that of PTAA:Li-TFSI/t-BP (30 mV). The corresponding RMS values of PTAA:Li-TFSI/t-BP and PTAA:PFB-TFSI films are 6.5 and 5.2 mV, respectively. The reduced RMS of PTAA:PFB-TFSI film indicates that the uniformity of surface potential is enhanced, which is beneficial for improving the charge transfer efficiency and enhancing the device efficiency.

In addition, the stabilities of perovskite covered with PTAA:Li-TFSI/t-BP and PTAA:PFB-TFSI films were tested using XRD[45, 46]. As shown in Figure S9, samples show the typical diffraction peaks of perovskite films. Due to the hygroscopic nature of Li-TFSI and the presence of pores in the film, the Li-TFSI-doped samples exhibit distinct PbI_2 characteristic peaks after 15 days of aging, indicating perovskite degradation. In contrast, after aging for 15 days, no obvious PbI_2 characteristic peak is observed in the PFB-TFSI-doped samples. To further investigate the degradation process of perovskite films, 2D Grazing Incidence X-ray Diffraction (2D-GIXD) of the relevant samples with ITO/SnO_2/perovskite/HTL structure was performed. As shown in Figures 4e and 4f, after aging for 30 days at 23 ± 4 °C with 50-70% relative humidity in air, the samples doped with PFB-TFSI and Li-TFSI/t-BP exhibit diffraction rings with different intensities at $q \approx 10$, 20, and 23.5 nm^{-1}, corresponding to the (110), (220),

View Article Online
DOI: 10.1039/D5SC04440E

and (310) crystal planes of perovskite, respectively. Compared to the PTAA:PFB-TFSI samples, the PTAA:Li-TFSI/t-BP samples show a clearer and more distinct diffraction ring at $q \approx 9\ nm^{-1}$, which is related to the degradation of perovskite and the formation of PbI_2. These results demonstrate that due to the non-ionic structure and hydrophobicity of PFB-TFSI, as well as its solubility in chlorobenzene, the PTAA:PFB-TFSI film has a smoother and more uniform surface morphology compared to the PTAA:Li-TFSI/t-BP film. It effectively blocks the intrusion of water molecules to protect the perovskite layer, thereby ensuring good long-term stability of PSCs based on PTAA:PFB-TFSI.

3. Conclusion

In summary, a novel fluorinated molecule PFB-TFSI is developed as a p-dopant for PTAA in PSCs. PFB-TFSI has good solubility and hydrophobicity, and its lower HOMO level can directly oxidize PTAA to generate $[PTAA]^+$ radical cations without post-treatment. In addition, F and O atoms in PFB-TFSI can passivate perovskite defects. Compared to 21.98% PCE of PSC based on PTAA:Li-TFSI/t-BP, PSC based on PTAA:PFB-TFSI achieved a higher PCE of 24.22%. Moreover, the long-term stability of PSC based on PTAA:PFB-TFSI is greatly improved, retaining 90% of its initial PCE after aging for 30 days at 23 ± 4 °C and 50-70% relative humidity, whereas PSC based on PTAA:Li-TFSI/t-BP only retains 57%. Furthermore, after aging for 300 hours at 85 °C in ambient air with 50-70% relative humidity, PSC based on PTAA:PFB-TFSI maintained 88% of its initial PCE, while PSC based on PTAA:Li-TFSI/t-BP retained only 63%. This work successfully developed a non-ionic p-dopant based on Li-TFSI structure, achieving effective doping of PTAA and ultimately improving the efficiency and long-term stability of PSCs.

Data availability

The data that support the findings of this study are available in the ESI.

Conflicts of interest

The authors declare no conflict of interest.

View Article Online
DOI: 10.1039/D5SC04440E

Acknowledgements

The authors are grateful to the National Natural Science Foundation of China (No. 62374029, 22175029, 62474033 and W2433038), the Young Elite Scientists Sponsorship Program by CAST (No. YESS20220550), the Sichuan Science and Technology Program (No. 2024NSFSC0250), the Natural Science Foundation of Shenzhen Innovation Committee (JCYJ20210324135614040) and the Fundamental Research Funds for the Central Universities of China (No. ZYGX2022J032).

References

[1] A. Kojima, K. Teshima, Y. Shirai, et al. Organometal Halide Perovskites as Visible-Light Sensitizers for Photovoltaic Cells. *Journal of the American Chemical Society* **2009**, 131, 6050-6051.

[2] H. Oga, A. Saeki, Y. Ogomi, et al. Improved Understanding of the Electronic and Energetic Landscapes of Perovskite Solar Cells: High Local Charge Carrier Mobility, Reduced Recombination, and Extremely Shallow Traps. *Journal of the American Chemical Society* **2014**, 136, 13818-13825.

[3] J. Lim, M. T. Hörantner, N. Sakai, et al. Elucidating the long-range charge carrier mobility in metal halide perovskite thin films. *Energy & Environmental Science* **2019**, 12, 169-176.

[4] S. D. Stranks, G. E. Eperon, G. Grancini, et al. Electron-Hole Diffusion Lengths Exceeding 1 Micrometer in an Organometal Trihalide Perovskite Absorber. *Science* **2013**, 342, 341-344.

[5] J. Park, J. Kim, H.-S. Yun, et al. Controlled growth of perovskite layers with volatile alkylammonium chlorides. *Nature* **2023**, 616, 724-730.

[6] National Renewable Energy Laboratory. Best research-cell efficiency chart. https://www.nrel.gov/pv/cell-efficiency.html.

[7] J. X. Xia, J. S. Luo, H. Yang, et al. Vertical Phase Separated Cesium Fluoride Doping Organic Electron Transport Layer: A Facile and Efficient "Bridge" Linked Heterojunction for Perovskite Solar Cells. *Advanced Functional Materials* **2020**, 30, 2001418.

[8] Y. B. Wang, Y. F. Yue, X. D. Yang, et al. Toward Long-Term Stable and Highly Efficient Perovskite Solar Cells via Effective Charge Transporting Materials. *Advanced Energy Materials* **2018**, 8, 1800249.

[9] Z. Xing, S. H. Li, S. H. Yang, et al. Targeted Molecular Design of Functionalized Fullerenes for High-Performance and Stable Perovskite Solar Cells. *Small Structures* **2022**, 3, 2200012.

[10] J. Burschka, N. Pellet, S. J. Moon, et al. Sequential deposition as a route to high-performance perovskite-sensitized solar cells. *Nature* **2013**, 499, 316-319.

[11] L. Calió, S. Kazim, M. Grätzel, et al. Hole-Transport Materials for Perovskite Solar Cells. *Angewandte Chemie International Edition* **2016**, 55, 14522-14545.

[12] M. Kim, J. Jeong, H. Lu, et al. Conformal quantum dot-SnO_2 layers as electron transporters for efficient perovskite solar cells. *Science* **2022**, 375, 302-306.

[13] J. Jeong, M. Kim, J. Seo, et al. Pseudo-halide anion engineering for α-$FAPbI_3$ perovskite solar cells. *Nature* **2021**, 592, 381-385.

[14] H. Min, M. Kim, S.-U. Lee, et al. Efficient, stable solar cells by using inherent bandgap of α-phase formamidinium lead iodide. *Science* **2019**, 366, 749-753.

[15] J. J. Yoo, G. Seo, M. R. Chua, et al. Efficient perovskite solar cells via improved carrier management. *Nature* **2021**, 590, 587-593.

[16] Z. Li, C. Xiao, Y. Yang, et al. Extrinsic ion migration in perovskite solar cells. *Energy & Environmental Science* **2017**, 10, 1234-1242.

[17] S. Wang, Z. Huang, X. Wang, et al. Unveiling the Role of tBP-LiTFSI Complexes in Perovskite Solar Cells. *Journal of the American Chemical Society* **2018**, 140, 16720-16730.

[18] W. Li, H. Dong, L. Wang, et al. Montmorillonite as bifunctional buffer layer material for hybrid perovskite solar cells with protection from corrosion and retarding recombination. *Journal of Materials Chemistry A* **2014**, 2, 13587-13592.

[19] S. Wang, M. Sina, P. Parikh, et al. Role of 4-tert-Butylpyridine as a Hole Transport Layer Morphological Controller in Perovskite Solar Cells. *Nano Letters* **2016**, 16, 5594-5600.

[20] J. Zhang, T. Zhang, L. Jiang, et al. 4-tert-Butylpyridine Free Hole Transport Materials for Efficient Perovskite Solar Cells: A New Strategy to Enhance the Environmental and Thermal Stability. *ACS Energy Letters* **2018**, 3, 1677-1682.

[21] N. A. N. Ouedraogo, G. O. Odunmbaku, B. Guo, et al. Oxidation of Spiro-OMeTAD in High-Efficiency Perovskite Solar Cells. *ACS Applied Materials & Interfaces* **2022**, 14, 34303-34327.

[22] X. Liu, B. Zheng, L. Shi, et al. Perovskite solar cells based on Spiro-OMeTAD stabilized with

View Article Online
DOI: 10.1039/D5SC04440E

an alkylthiol additive. *Nature Photonics* **2023**, 17, 96-105.

[23] J. Kong, Y. Shin, J. A. Röhr, et al. CO_2 doping of organic interlayers for perovskite solar cells. *Nature* **2021**, 594, 51-56.

[24] Luo, J. Xia, H. Yang, et al. Toward high-efficiency, hysteresis-less, stable perovskite solar cells: unusual doping of a hole-transporting material using a fluorine-containing hydrophobic Lewis acid. *Energy & Environmental Science* **2018**, 8, 2035-2045.

[25] N. Sakai, R. Warren, F. Zhang, et al. Adduct-based p-doping of organic semiconductors. *Nature Materials* **2021**, 20, 1248-1254.

[26] Y. Liu, Y. Hu, X. Zhang, et al. Inhibited aggregation of lithium salt in spiro-OMeTAD toward highly efficient perovskite solar cells. *Nano Energy* **2020**, 70, 104483.

[27] X. Guo, J. Li, B. Wang, et al. Improving and Stabilizing Perovskite Solar Cells with Incorporation of Graphene in the Spiro-OMeTAD Layer: Suppressed Li Ions Migration and Improved Charge Extraction. *ACS Applied Energy Materials* **2020**, 3, 970-976.

[28] L.-L. Jiang, Z.-K. Wang, M. Li, et al. Flower-like MoS_2 nanocrystals: a powerful sorbent of Li^+ in the Spiro-OMeTAD layer for highly efficient and stable perovskite solar cells. *Journal of Materials Chemistry A* **2019**, 8, 3655-3663.

[29] H. Zhang, Y. Shi, F. Yan, et al. A dual functional additive for the HTM layer in perovskite solar cells. *Chemical Communications* **2014**, 39, 5020-5022.

[30] K. Wang, X. Liu, R. Huang, et al. Nonionic $Sc_3N@C_{80}$ Dopant for Efficient and Stable Halide Perovskite Photovoltaics. *ACS Energy Letters* **2019**, 20, 1852-1861.

[31] J.-Y. Seo, H.-S. Kim, S. Akin, et al. Novel p-dopant toward highly efficient and stable perovskite solar cells. *Energy & Environmental Science* **2018**, 10, 2985-2992.

[32] C. Ming, A. Kerttu, C. Cheng, et al. Acceptor-Donor-Acceptor Type Ionic Molecule Materials for Efficient Perovskite Solar Cells and Organic Solar Cells. *Nano Energy* **2016**, 30, 387-397.

[33] D. Vaitukaityte, C. Momblona, K. Rakstys, et al. Cut from the Same Cloth: Enamine-Derived Spirobifluorenes as Hole Transporters for Perovskite Solar Cells. *Chemistry of Materials* **2021**, 33, 6059-6067.

[34] F. Ali, C. Roldán-Carmona, M. Sohail, et al. Applications of Self-Assembled Monolayers for Perovskite Solar Cells Interface Engineering to Address Efficiency and Stability. *Advanced Energy Materials* **2020**, 13, 2002989.

[35] B. de Boer, A. Hadipour, M. M. Mandoc, et al. Tuning of Metal Work Functions with Self-Assembled Monolayers. *Advanced Materials* **2005**, 17, 621-625.

[36] F. Ansari, E. Shirzadi, M. Salavati-Niasari, et al. Passivation mechanism exploiting surface dipoles affords high-performance perovskite solar cells. *Journal of the American Chemical Society* **2020**, 26, 11428-11433.

[37] H. Zhang, F. T. Eickemeyer, Z. Zhou, et al. Multimodal host–guest complexation for efficient and stable perovskite photovoltaics. *Nature Communications* **2021**, 12, 3383.

[38] D. Wei, F. Ma, R. Wang, et al. Ion-Migration Inhibition by the Cation-π Interaction in Perovskite Materials for Efficient and Stable Perovskite Solar Cells. *Advanced Materials* **2018**, 30, 1707583.

[39] R. C. Shallcross, S. Olthof, K. Meerholz, et al. Impact of Titanium Dioxide Surface Defects on the Interfacial Composition and Energetics of Evaporated Perovskite Active Layers. *ACS Applied Materials & Interfaces* **2019**, 11, 32500-32508.

[40] Y.-S. Jeon, D.-H. Kang, J.-H. Kim, et al. Stability and efficiency improvement of perovskite solar cells by surface hydroxyl defect passivation of SnO_2 layer with 4-fluorothiophenol. *Journal of Materials Chemistry A* **2023**, 7, 3673-3681.

[41] X. Feng, B. Liu, Y. Peng, et al. Restricting the Formation of Pb-Pb Dimer via Surface Pb Site Passivation for Enhancing the Light Stability of Perovskite. *Small* **2022**, 18, 2201831.

[42] C. Liu, L. Zhang, Y. Li, et al. Highly Stable and Efficient Perovskite Solar Cells with 22.0% Efficiency Based on Inorganic-Organic Dopant-Free Double Hole Transporting Layers. *Advanced Functional Materials* **2020**, 30, 1908462.

[43] Y. R. Kim, C. M. Oh, C. J. Yoon, et al. Highly stable and efficient cathode-buffer-layer-free inverted perovskite solar cells. *Nanoscale* **2021**, 11, 5652-5659.

[44] J. Zhang, Y. Hua, B. Xu, et al. The Role of 3D Molecular Structural Control in New Hole Transport Materials Outperforming Spiro-OMeTAD in Perovskite Solar Cells. *Advanced Energy Materials* **2016**, 6, 1601062.

[45] Q. Chen, J. Wu, X. Wang, et al. 3-Chloroperoxybenzoic acid doping spiro-OMeTAD for improving the performance of perovskite solar cells. *Chemical Engineering Journal* **2022**, 450, 138313.

[46] M. Li, Z. K. Wang, Y. G. Yang, et al. Copper Salts Doped Spiro-OMeTAD for

High-Performance Perovskite Solar Cells. *Advanced Energy Materials* **2016**, 6, 1601156.

View Article Online
DOI: 10.1039/D5SC04440E

View Article Online
DOI: 10.1039/D5SC04440E

Data Availability Statement

The data supporting this article have been included in the manuscript.